235 +
1/16/79

Ω. 2069

DOE/JPL/954376-6

LASER-ZONE GROWTH IN A RIBBON-TO-RIBBON (RTR) PROCESS SILICON
SHEET GROWTH DEVELOPMENT FOR THE LARGE AREA SILICON SHEET
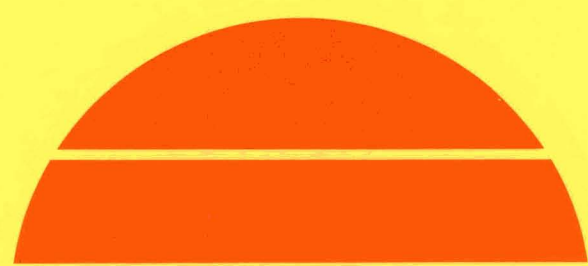TASK OF THE LOW COST SILICON SOLAR ARRAY PROJECT

Technical Quarterly Report No. 8, April 1—June 30, 1978

By
A. Baghdadi
R. W. Gurtler
R. Legge
B. Sopori
R. J. Ellis

Work Performed Under Contract No. NAS-7-100-954376

MASTER

Semiconductor Group
Motorola Incorporated
Phoenix, Arizona

U.S. Department of Energy

Solar Energy

DISCLAIMER

This report was prepared as an account of work sponsored by an agency of the United States Government. Neither the United States Government nor any agency Thereof, nor any of their employees, makes any warranty, express or implied, or assumes any legal liability or responsibility for the accuracy, completeness, or usefulness of any information, apparatus, product, or process disclosed, or represents that its use would not infringe privately owned rights. Reference herein to any specific commercial product, process, or service by trade name, trademark, manufacturer, or otherwise does not necessarily constitute or imply its endorsement, recommendation, or favoring by the United States Government or any agency thereof. The views and opinions of authors expressed herein do not necessarily state or reflect those of the United States Government or any agency thereof.

DISCLAIMER

Portions of this document may be illegible in electronic image products. Images are produced from the best available original document.

LASER-ZONE GROWTH IN A RIBBON-TO-RIBBON (RTR) PROCESS
SILICON SHEET GROWTH DEVELOPMENT FOR THE LARGE AREA
SILICON SHEET TASK OF THE LOW COST SILICON SOLAR
ARRAY PROJECT

TECHNICAL QUARTERLY REPORT NO. 8

Motorola Report No. 2256/10

1 April 1978 - 30 June 1978

MASTER

JPL CONTRACT NO. 954376

BY

A. BAGHDADI

PRINCIPAL INVESTIGATOR

R. W. GURTLER, R. LEGGE, B. SOPORI, R. J. ELLIS

PREPARED BY

MOTOROLA INC. SEMICONDUCTOR GROUP
5005 E. McDowell Road
Phoenix, Arizona 85008

Motorola Project No. 2319 - 2325

TABLE OF CONTENTS

LIST OF FIGURES

LIST OF TABLES

SUMMARY

Further progress in growth rate has bee made, reaching an area throughput rate of 38 cm^2/min. This growth rate was achieved, using CVD feedstock, both with a 7.6 cm wide ribbon grown at 5 cm/min and a 5 cm wide ribbon grown at 7.6 cm/min. The 5 cm wide ribbon exhibited a dendritic structure; although the ribbon showed a tendency to buckle in the non-dendritic region, it was perfectly flat once the dendrites were firmly established. The 7.6 cm wide ribbon was non-dendritic, and had severe buckling. We have also demonstrated multiple ribbon growth (three 2.5 cm wide ribbons grown at 2.5 cm/min) and growth using the continuous system.

A new design for an improved furnace for RTR growth has been completed. The main design emphasis was to reduce complexity of the furnace, improve ease of maintenance, and extend the useful life of the furnace. We are also investigating the use of high purity Al_2O_3, BeO, and Si_3N_4 for the furnace support plates. Si_3N_4 also appears to be a promising alternative to quartz for the ribbon shroud.

The semi-continuous polysilicon CVD ribbon reactor has been designed and is being assembled and tested. A single ribbon ~ 2" x 28" was grown on a stationary Mo belt in this furnace.

A study of the microstructure of dendrites growing in RTR ribbon has shown that they contain a small, usually even, number of parallel twins. The dendrites themselves do not have a measurable effect on the ribbon's photo-response. We have shown that a prevalent defect structure in silicon ribbon consists of stacking faults (rather than grown-in twin boundaries). These stacking faults are generated in the bulk of the ribbon after solidification.

Electrical activity of defects in RTR ribbon has been studied by
fabricating an array of photodiodes on the ribbon, and using an SEM in the
electron beam induced current (EBIC) mode. We have concluded that, although
grain boundaries serve as effective recombination centers, they do not occur
frequently enough to greatly reduce the generation current in a structure as
large as a solar cell. Dislocation densities must exceed $10^6/cm^2$ in order
to strongly reduce the photoresponse of a solar cell.

We have fabricated our first solar cell on RTR ribbon grown from CVD
feedstock. The overall efficiency was 6.7%, with I_{SC} = 24 mA/cm^2, V_{OC} = 0.53
volts, fill factor = 0.53. Total cell area was 2.5 cm^2.

The Mo impurity level was measured in a few CVD samples by Neutron Activation
analysis. This analysis indicated a Mo level of 5 - 10 ppm in the bulk of
the silicon ribbon.

The YAG laser was used for RTR growth. Its sensitivity to module alignment
and positioning made it too difficult to operate continuously, so further work
will proceed using the CO_2 lasers.

1.0   GROWTH USING YAG LASERS

Figure 1 is a comparison of the power requirements of the CO_2 and YAG lasers. The ratio of the slopes shows a factor of ~ 5.6 in favor of the YAG lasers. From the point of view of energy utilization, the two systems are equivalent: the higher coupling efficiency of the YAG system is roughly counterbalanced by the overall higher efficiency of the CO_2 laser (~ 10%) compared to YAG lasers (1 - 2%).

The cost of a multi-kilowatt CO_2 laser is projected at $30/watt in moderate (10 systems/year) quantities. The YAG lasers are roughly twice as expensive ~ $60/watt. So for a given throughput, the YAG system would actually need less capital investment. However, the maitenance cost of the YAG system would be much higher (> $1/hour-module) so that the overall cost-effectiveness of YAG lasers would not be necessarily attractive.

The most important factor at this time, however, is reliability. The YAG systems at present use 3 modules to deliver a total of ~ 375/watts system. The alignment and positioning of these modules are critical to overall power output. This sensitivity, aggravated by the need for frequent lamp replacement, made it almost impossible to operate the YAG systems at their maximum rated power.

Our conclusion is that although the YAG lasers have a potential advantage in terms of capital investment, their lack of reliability (in high power systems) eliminates them from consideration at this time. If a single module, high power (> 500 watts) YAG laser with demonstrable reliability is developed, it would become a candidate laser for the RTR process. Until then, the CO_2 laser is a proven, cost-effective source of radiation for RTR silicon ribbon growth.

RIBBON THICKNESS 250μm
RIBBON WIDTH 2.5 cm

X CO_2 Lasers
O   YAG Lasers

POWER REQUIRED (WATTS)

1200

Slope: 124 watts/cm/min

800

400

Slope: 22 watts/cm/min

2   4   6   8

Feed Rate (cm/min)
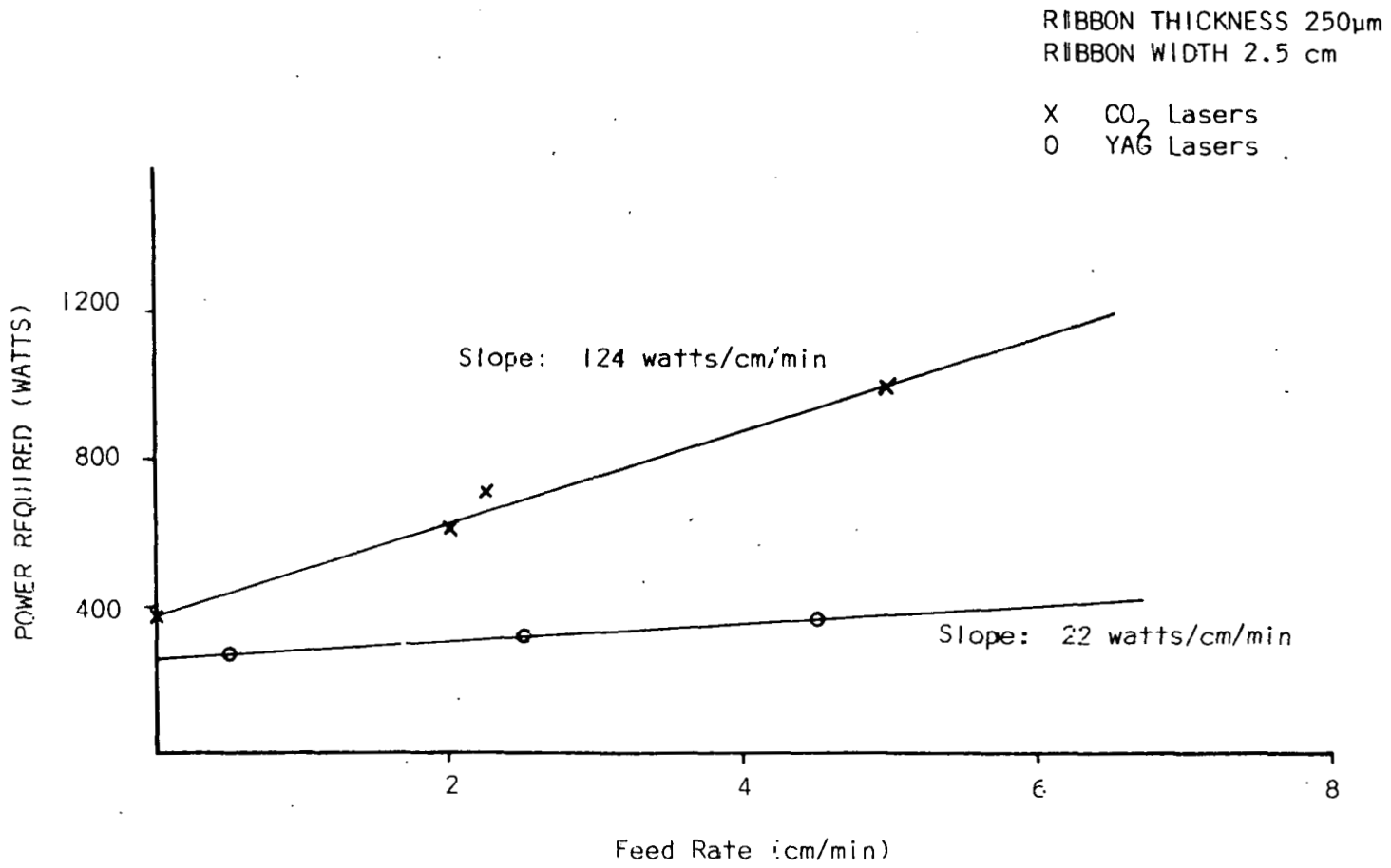
FIGURE 1:   COMPARISON OF POWER REQUIREMENTS USING CO_2 LASERS AND YAG
             LASERS (WITHOUT PRE-HEATERS).

2.0   CRYSTAL GROWTH

Addition of a pre-heater (See Section 3.0) to the crystal growth station has enabled us to demonstrate some important milestones in ribbon growth.

Using 250 micron thick CVD feedstock we have grown 5 cm wide ribbon at growth rates up to 7.6 cm/min. Close examination of a 5 cm-wide ribbon grown at 7.6 cm/min showed that, although it had a tendency to buckle in the non-dendritic region, the buckling was eliminated in the dendritic region. Figure 2A is a photo of this sample. Note that, compared to dendritic ribbons grown from 2.5 cm-wide feedstock, the dendrites on the 5 cm wide ribbon are somewhat more regular. This indicates a relatively flat solid-liquid interface across the ribbon width.

We have succeeded in RTR ribbon growth from 7.6 cm wide CVD feedstock (See Figure 2B). The growth rate was 5 cm/min and the total length grown was 15 cm. This ribbon was grown in the ratio (2:1) mode; thus, since the feedstock thickness was ~ 8 mils, the grown ribbon thickness ~ 4-5 mils. Hence, an area rate of growth of 38 cm^2/min has been achieved using both 5 cm-wide and 7.6 cm-wide CVD feedstock.

The practicability of multiple ribbon growth was demonstrated by growing three 2.5 cm-wide ribbons at 2.5 cm/min. The growth was routine; it did not present any additional difficulties compared to growth of a single 2.5 cm wide ribbon.

The new crystal growth station, RTR #2 is now operational. Ribbon growth using the continuous roller system was carried out with 2.5 cm wide feedstock. The length of the re-crystallized ribbon was 7 cm, and the growth rate was 2.5 cm/min. This brief experiment did not uncover any significant problems with the operation of the continuous ribbon system.
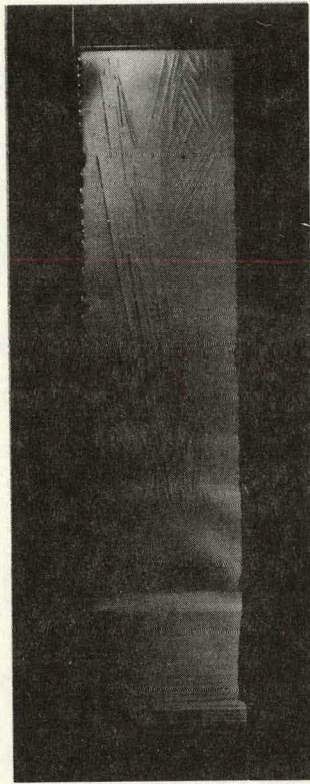
Figure 2A.   Dendritic Ribbon
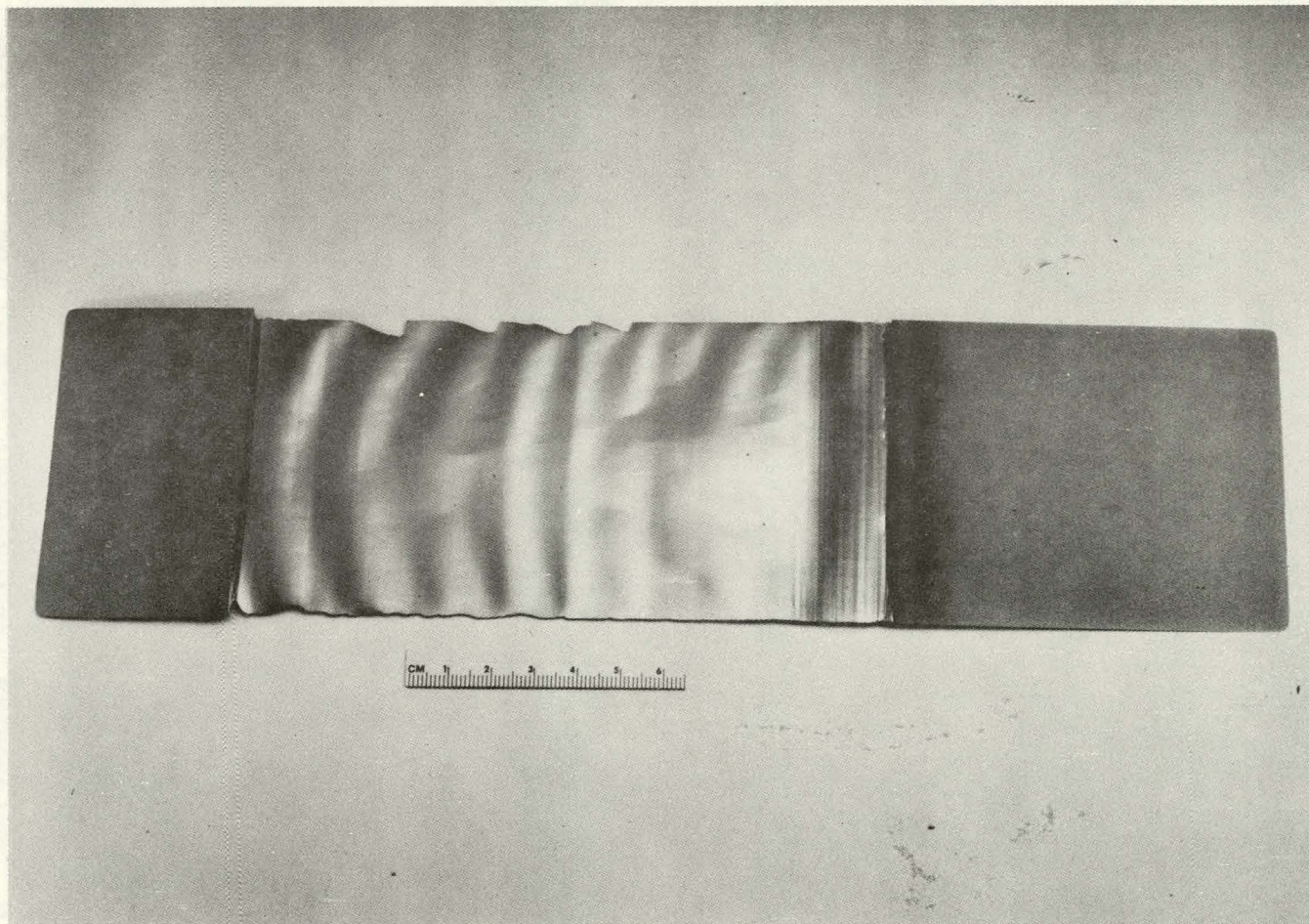
FIGURE 2b: RTR RIBBON

3.0 FURNACE DEVELOPMENT

3.1 PRE-HEATER - POST-HEATER COMBINATION AND BUCKLING EFFECTS

As discussed in Section 4.6 of the 7th Technical Quarterly Report, the type of temperature profile now being utilized for wide ribbon growth is indicated in Figure 3. To achieve this profile, a pre-heater (with pre-heater controller) was built along similar designs as the present post-heater. The pre-heater was attached piggyback style to the existing post-heater. Provision was made to allow variable separation between the pre-and post-heater assemblies in order to control the plateau temperature level and to ensure unobstructed access of the laser beams to the melt region.

The use of this type of temperature profile was dicated by increased fracture and buckling problems as the sample width became larger. In discussing buckling problems as applied to RTR growth, it is necessary to differentiate two observed buckling effects. The first (and perhaps more unique to RTR growth) is a long wavelength buckling which is manifested in a difficulty to maintain an unmelted ribbon in a flat condition. Upon insertion into the growth furnace, large radius-of-curvature buckling can result which makes growth difficult or impossible because of interference with furnace walls, etc. The second type of buckling is the periodic, shorter wavelength variety observed in grown ribbons and is the type reported by other ribbon growth researchers.

Results of the use of this heater combination have been positive; wide ribbon growth has been achieved with reduced buckling tendencies and reduced fracture probabilities. Long wavelength buckling does still occur, however, and this appears to be primarily due to the nonlinear temperature profiles at the cool ends of the pre- and post-heaters; the profiles within
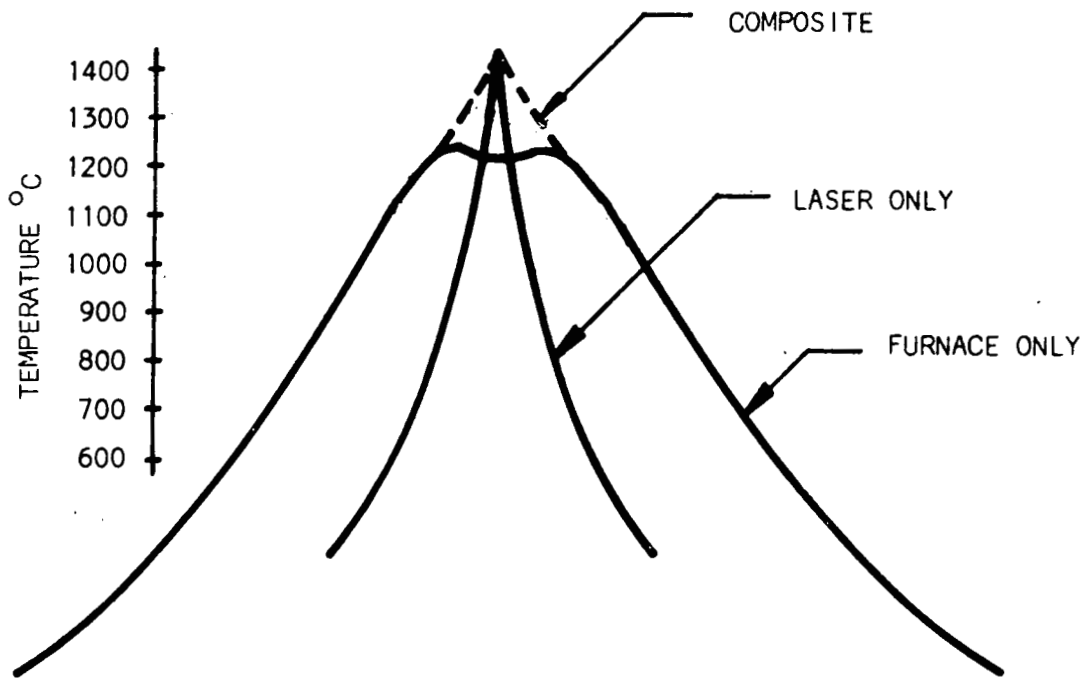
FIGURE 3:   THERMAL PROFILES FOR A PREHEATER AND POSTHEATER
              COMBINATION WITH LINEAR PROFILE REGIONS BELOW
              APPROXIMATELY 1200°C.

the furnace together with the occurrence of a plastic region at the nonlinear peak temperature region should not lend to buckling, but the nonlinear entrance and exit regions can cause buckling. Observations tend to confirm this explanation: upon initial insertion of a ribbon, buckling occurs almost immediately after entering the operating furnace. After the ribbon has been completely established within the furnace, the amount of buckling has been observed to decrease.

Theoretically, the critical stress for buckling is strongly dependent not only on the dimensions of the sample, but also on the location of any physical constraints in relation to the stressed region. In particular, if we can impose on the ribbon a constraint to be flat close to the stressed region, buckling should be strongly inhibited. Consequently, guide structures are being designed to attach to the pre- and post-heaters which will physically constrain the ribbons to be flat at the entrance and exit of the heater assembly. Once the ribbon is inside the furnace, no buckling stresses should be present and, as a result, it is hoped that this long wavelength buckling problem will be greatly alleviated.

3.2   NEW DESIGNS

Design has been completed on a new furnace for routine RTR growth. While the design is similar to that of our previous furnace, numerous changes have been made to "standardize" the parts, improve ease of maintenance, and to extend the useful life of the furnace. Some of the major features of the new furnace are:

.   Symmetrical and interchangeable pre-heater and post-heater sections.

.   Use of a simpler heating element support concept employing an inexpensive slotted support plate with numerous replaceable refractory plates

8

(which support the heating elements) mounted in the slots.

. Provision for the rapid replacement of any of the four heater sections.

. Remote and separate control of the position of the pre-heater and post-
heater sections.

Since much of our down-time in the past can be attributed to furnace or furnace controller failures and lack of back-up units, we are constructing several extra furnaces and furnace controllers.

Figure 4 is a cross section of the furnace illustrating the heater element support plates, the heater elements, and the refractory (quartz) shroud which protects the ribbon from possible heater element evaporation. Because of high temperatures in the vicinity of the melt and the numerous temperature cycles, we have had a severe problem of thermal fatigue in the ribbon shroud and support plates. The ribbon shroud is presently fabricated from quartz while the support elements have been made from high-alumina-content ceramics. The quartz has rapidly devitrified (due to the numerous temperature cycles involved in an R&D environment) and the alumina has not been able to handle the thermal stresses -- resulting in fracture.

To combat these problems, we are investigating alternative refractories. For the individual support plates, high purity Al_2O_3, Si_3N_4 and BeO will be investigated. In yet a new design, the support plates are independent and held in a slotted-member; they are roughly at a uniform temperature lengthwise. Free expansion along the length should prevent fracture of these parts. For the ribbon shroud, Si_3N_4 appears to be a reasonable alternative to quartz, although quartz will continue to find use due to its relative ease of fabrication.

GROWTH
DIRECTION

SILICON RIBBON

SUPPORT
PLATE

COOLING
TUBE

HEATER
ELEMENTS

QUARTZ
SHROUD
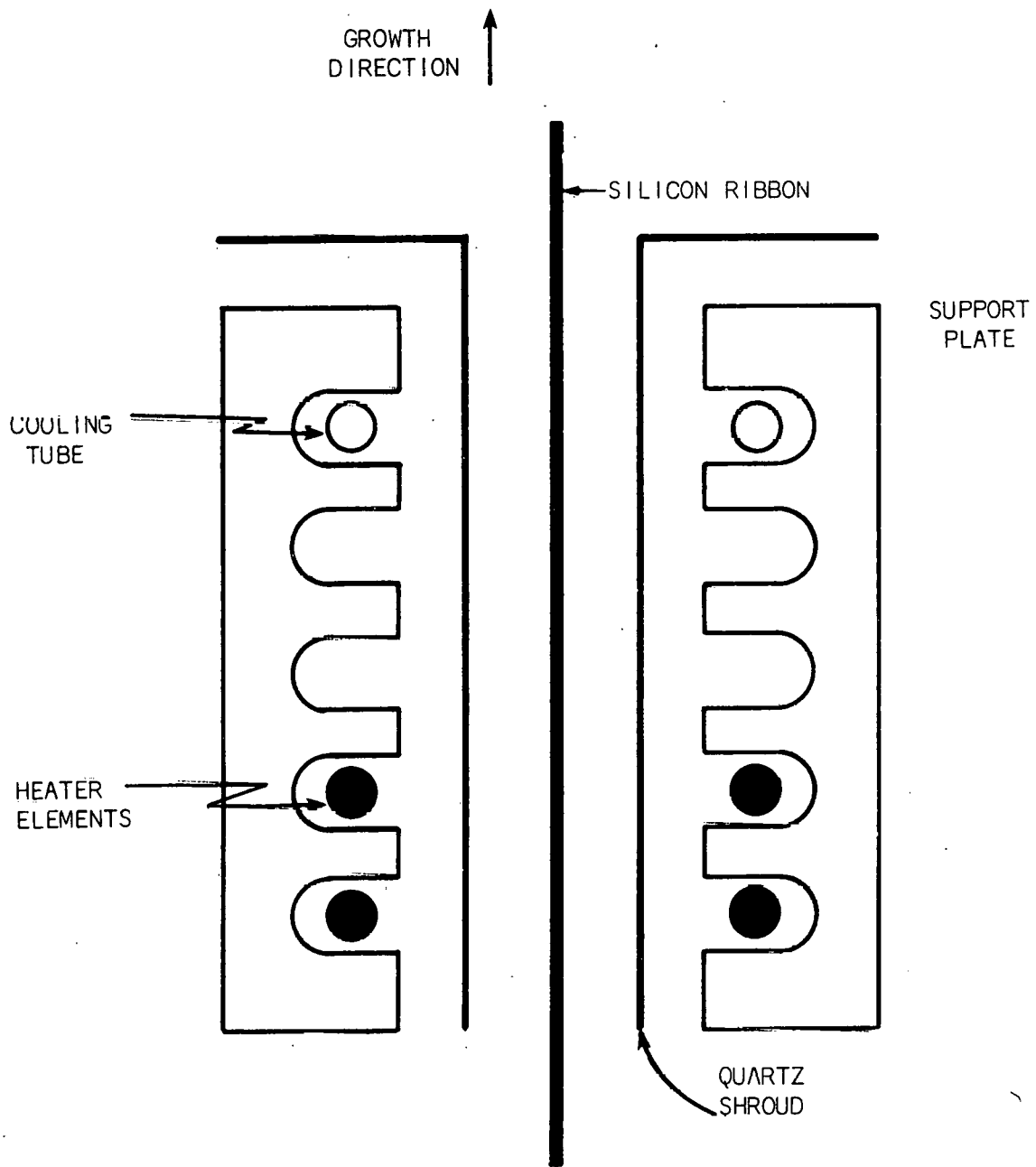
Figure 4 .   Furnace Cross-Section

10

4.0   STRESS ANALYSIS

Ribbon buckling, high dislocation densities, and residual stresses are all results of the thermal stresses acting on the ribbon during growth. Residual stresses may be eliminated through use of a post-heater with a linear temperature profile if the post-heater parameters are correctly chosen. However, as repeatedly mentioned, adequate stress relief demands a linear profile with a relatively small gradient. High growth rates, however, demand a steep gradient. This dichotomy of requirements has been met by those working in the field by the acceptance of a two-zone post-solidification temperature profile: a transition zone between the molten region and the post-heater which has a high thermal gradient, and the post-heater zone itself which has a shallow gradient. Inevitably, however, this combination leads to large $\partial_x^2 T$ induced stresses in the transition region, and ribbon buckling is a consequence. Also, relief of these stresses through plastic flow results in the generation of stacking faults and high dislocation densities.

Because of the need for a better understanding of the distribution and magnitude of thermal stresses as a function of the numerous thermal profile parameters, a program for the numerical solution of the two dimenstional plane stress equations has been developed. This program solves the biharmonic equation, reference (1)

$$\nabla^4 \phi = -\alpha E \nabla^2 T \qquad (1)$$

where ϕ is the Airy stress function, α is the thermal expansion coefficient and E is Young's modulus. T may be a function of X and Y. The solution is obtained through utilization of the finite difference approximation of (1) in an arbitrary rectangular net and use of a Liebman relaxation process. Assumed geometry for the solution is indicated in Figure 5. A semi-infinite strip of width 2C is assumed; further assumptions are that the temperature distribution

11
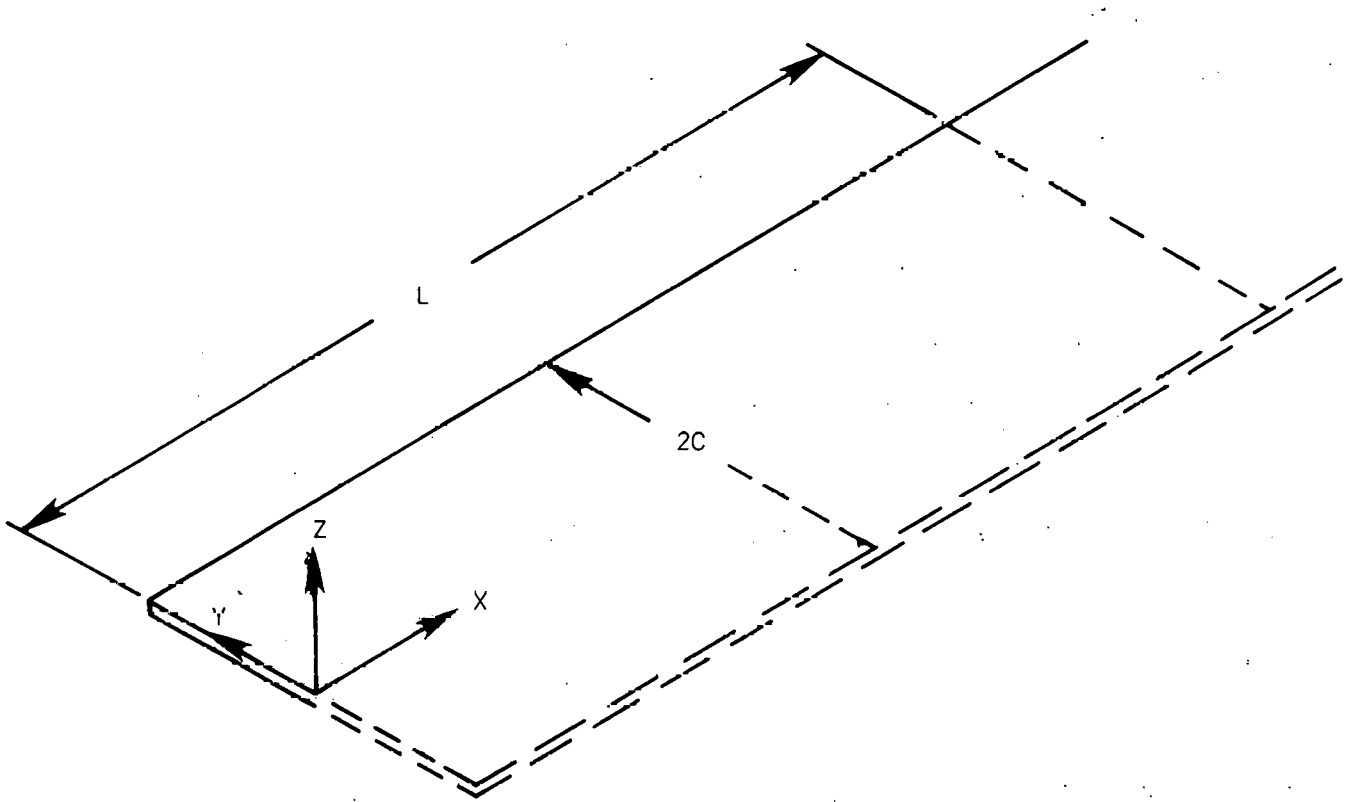
FIGURE 5: GEOMETRY USED IN STRESS ANALYSIS

(and therefore the stresses) is symmetrical about y =) and that all edges

are traction free. The stresses are given by

$$\sigma_{xx} = \partial_y^2 \phi$$

$$\sigma_{xy} = \partial_{xy}^2 \phi$$

$$\sigma_{yy} = \partial_x^2 \phi$$

and the traction-free edges imply that on the edges,

$$\phi = \partial_n \phi = 0$$

where n implies the normal direction. To generate a boundary conditon for

X = L, where L is the maximum dimension computed, $\phi(L,y)$ is chosen to equal

the exact solution for a region far from the ends of a rectangular strip under

the influence of a gently varying temperature distribution of parabolic

dependence (or less) in X. Only temperature distributions allowing this

assumption are utilized. However, the importance of this boundary condition is

not serious since a given region will, in general, influence only a region of

approximately ±2C from itself. Consequently, if X = L is at least 2C units

from the region of interest, little impact will result from the nature of the

solution at X = L.

Convergence of the relaxation process is presently relatively slow but

comparison of the results after the maximum residue has been reduced to 1 part

in 10^4 with an exact solution indicates accuracies within 10 - 20% for a

relatively coarse net. However high accuracy is not an essential requirement

at present since distributions and trends are of more interest.

Finally, it should be kept in mind that these solutions can only be a

guide to trends since the effects of plasticity are not accounted for.

Nevertheless, if a thermal profile could be conceived which will allow projected

stresses based on this elastic model to become small, it can safely be assumed

that significantly reduced buckling and generations of dislocations will result.

13

Discussion of Applications

At this time it is not useful to illustrate numerous graphical displays of stress distributions since our studies are not complete enough to present these in an illuminating manner. However, from preliminary work it is easy to verify the profound effects of the sample width on resulting stresses. The previously-mentioned influence zone of $\pm$ 2C from a strong temperature non-linearity becomes disturbingly large when 2C is 5 - 10 cm. Thus, a growth velocity-imposed thermal gradient requirement of perhaps 1000°C/cm and the ideal of a stress-free growth environment are totally incompatible since a severe temperature non-linearity must occur within ~ 1.5 cm from the melt (i.e., the constant temperature gradient must terminate).

In addition, the effects of placing strong non-linearities of temperature near the molten zone are also apparent. As the non-linearity approaches the molten zone, the longitudinal stresses (σ_{xx}) are damped while the lateral stresses (σ_{yy}) become very large in the immediate vicinity of the molten region.

Through these investigations we hope to identify the most favorable approach to stress reduction compatible with high growth rates. It can already be seen that an optimum ribbon width may be defined (assuming achievement of an ideal profile) which would provide substantial improvements in crystal quality due to stress reduction. Use of multiple ribbon growth would then allow the desired throughput to be achieved. Unfortunately this optimum width is relatively small, of the order of 1 cm, requiring growth of numerous ribbons. Furthermore, as long as crystal impurity appears to be the dominating factor in reductions of solar cell efficiency, such considerations are primarily of longer term interest.

14

5.0   CVD RIBBON FEEDSTOCK

Production of 1¼" x 9" x .010" polysilicon ribbon is currently being sustained full time on 2 R.F. epi reactors for one shift. Yielded out that translates into about 6 ribbons a day.

Arrangements are being made to expand the productivity by a factor of 2 by incorporating a second shift operation.

Development of the semi-continuous polysilicon ribbon reactor continues. Tests were performed on the newly designed end seals to determine whether or not they would contain the atmospheric integrity within the reactor. The tests included filling the chamber with anhydrous HCl and testing for external leaks with NH_4OH vapors. The other test was an examination for SiO_2 formation when Si was deposited in an ambient of H_2. Results from both tests indicate that atmospheric integrity within the chamber will be satisfactory to carry out ribbon growth.

We have also modified the end seals to accommodate a thicker (up to 0.020" molybdenum belt. The feed mechanism is now completed, and is ready for semi-continuous operation. We have installed a tachometer on the belt drive motor so that the belt speed may be observed continuously.

The first attempt at growth in the semi-continuous deposition chamber was very encouraging. This growth was carried out on a stationary belt. A single ribon, 28" long was recovered intact (See Figure 6). Ribbon thickness ranged from 1 to 10 mils, the width from 1½" to 2". This growth was carried out using $SiHCl_3$ in an H_2 ambient at $1150^{\circ}C$ on a 0.005" Moly belt. Since the ribbon exhibited wide variations in thickness, width and curvature (See Figure 6) we did not attempt to re-crystallize it in the RTR apparatus.
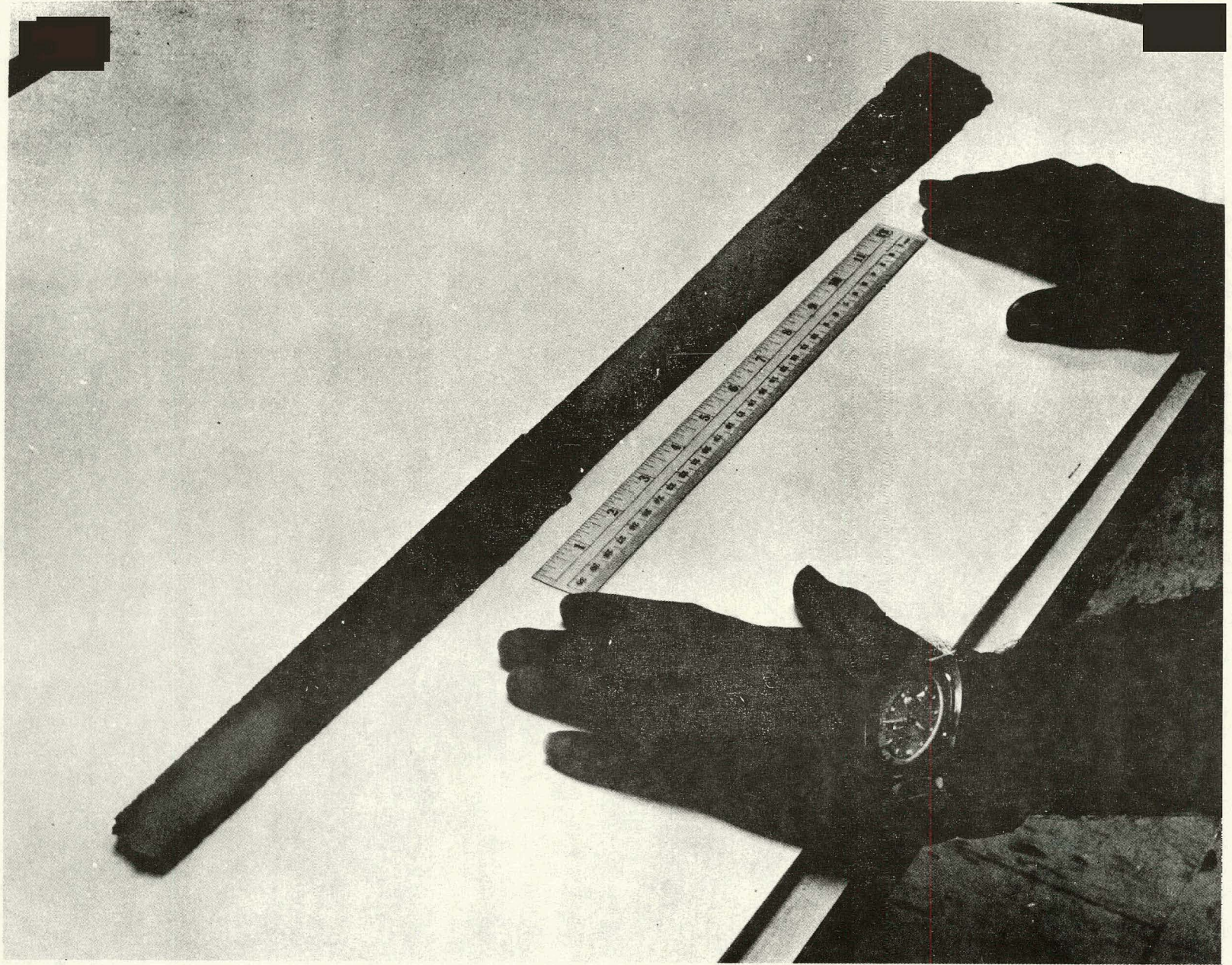
FIGURE 6: CVD RIBBON

6.0   DENDRITE STRUCTURE

Figure 2a is a photo of a ribbon grown in the dendritic regime. This 5 cm wide sample was grown at 7.6 cm/min. Note that before the dendritic regime was firmly established, the ribbon showed a tendency to buckle. The buckling virtually disappears in the dendritic ribbon. Figure 7 is a schematic of this sample, showing the position of selected Laue measurements.

The orientations of several grains were determined using a Laue camera. Grain "A" (See Figure 7) is ~3 mm wide, with a face F ~ (112) and a growth direction G ~ [513] and the expansion direction E ~ [131]. Grain "B" is 5 mm wide, with F ~ (311), G ~ [233] and E ~ [011]. Grain "C" is 4 mm wide with F ~ (223), G ~ [131] and E ~ [101]. In each case the growth direction of the dendrite itself was close to [112]. Thus in the dendritic regime the grain orientations are determined primarily by the dendritic growth requirements. The direction in which a dendrite grows is determined by the shape of the solid-liquid interface.

Figure 8 is an SEM view of the top surface of a dendrite. The ribbon was "texture etched" to reveal the differing orientations of the crystal grains. This dendrite contains a pair of twin planes, roughly ten microns apart. Note that the crystal orientations on both sides of the twin pair are identical. Figure 9a is an optical micrograph of a dendrite cross-section, showing a series of twin planes. This sample was etched 3 minutes in Wright etch to reveal its defect structure. Figure 9b is an SEM picture of the same dendrite. In this case the twin planes are ~ 6 μm apart. As a general rule, Laue photos show only a single orientation for each dendrite. Thus the dendrites usually contain an even number of parallel twins. In some cases (Orientation "B", Figure 7) the twin spacing was far enough apart (~ a fraction of a millimeter) to be revealed in the x-ray pattern.

17
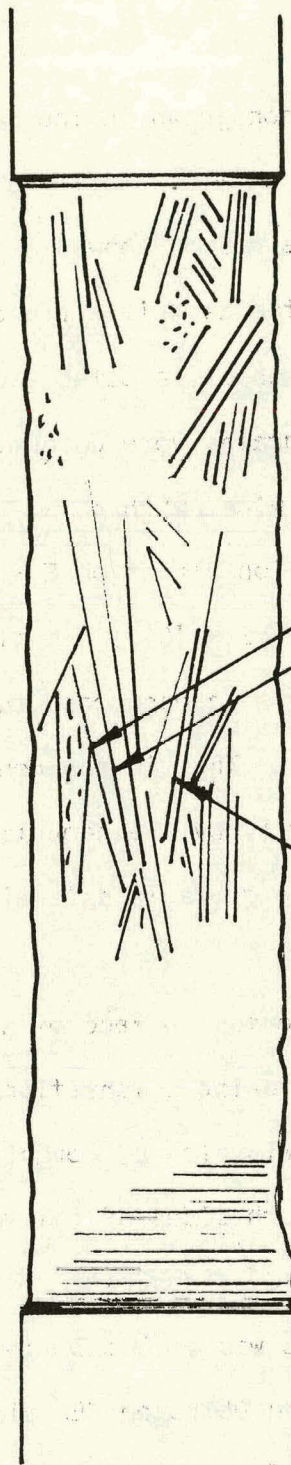
Figure 7.   Dendritic Ribbons. The lines represent
the dendrites. The crystallographic
orientation was measured at points A,B,C.
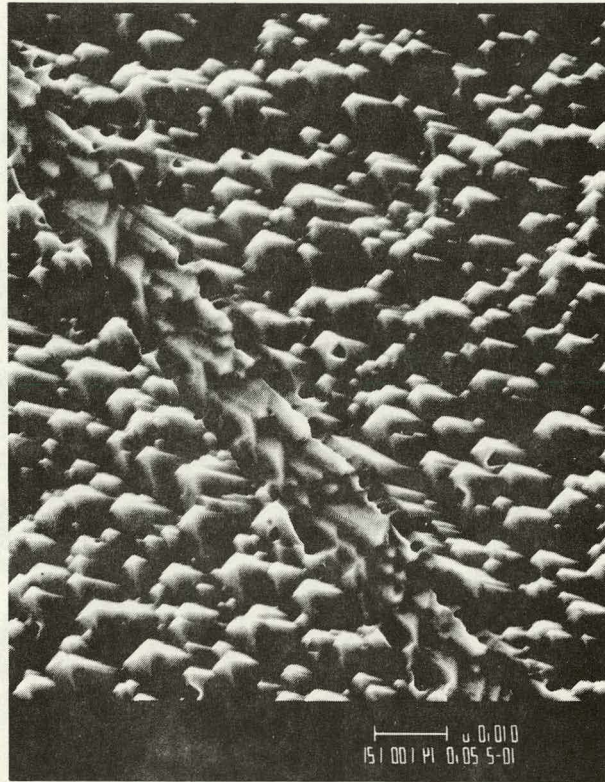
Figure 8.   Dendrite Surface
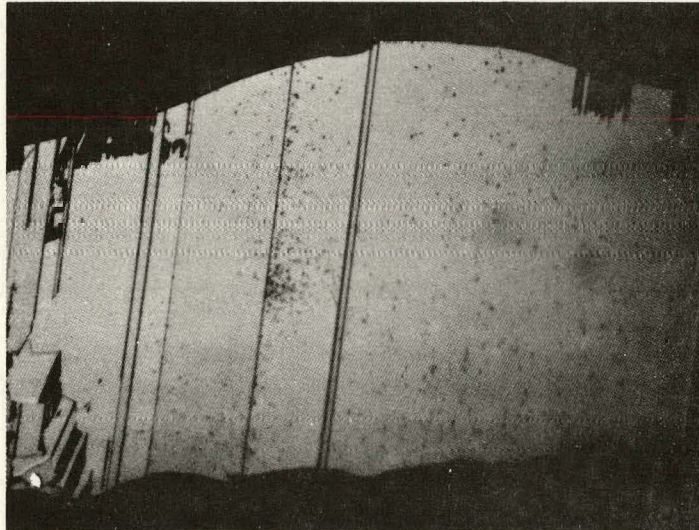
Figure 9a. Dendrite Cross-Section
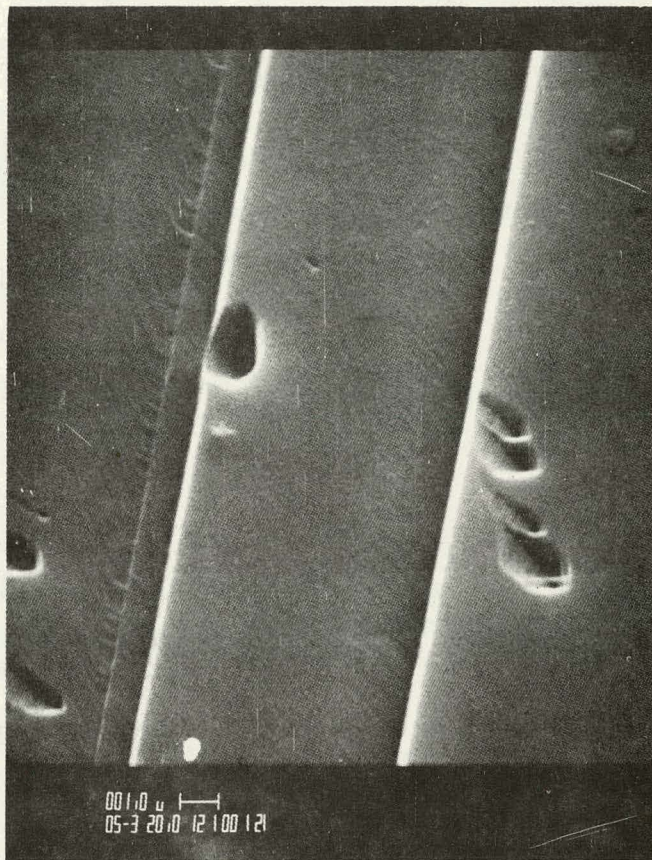
Figure 9b.   Dendrite Cross-Section

7.0   STACKING FAULTS

Figures 10, 11, 12 are micrographs showing defect structure in an RTR ribbon. In each case, the sample was etched for 3 minutes in Wright etch to delineate the defects. Figure 10 is an optical micrograph of the surface of the ribbon. This structure of dense planar defects has generally been referred to as a twin boundary structure (2). This micrograph clearly demonstrates that the predominant defect structure in silicon ribbons consists of stacking faults. The stacking faults usually end at a grain boundary, or the edge of the ribbon. In this case, however, the stacking fault is bounded by a pair of edge dislocations.

Figures 11 and 12 are SEM micrographs of sections of RTR ribbons taken from an area which contains a relatively high planar defect density. The section shown in Figure 11 was cut at right angles to the growth while the section shown in Figure 12 was cut parallel to the growth direction (and therefore parallel to the planar defects). Figure 12 clearly shows that these defects are stacking faults generated in the bulk of the ribbon after solidification. This is an important point because it indicates that the defect density might be reduced, if necessary, by controlling the temperature profile in the ribbon immediately after solidification.
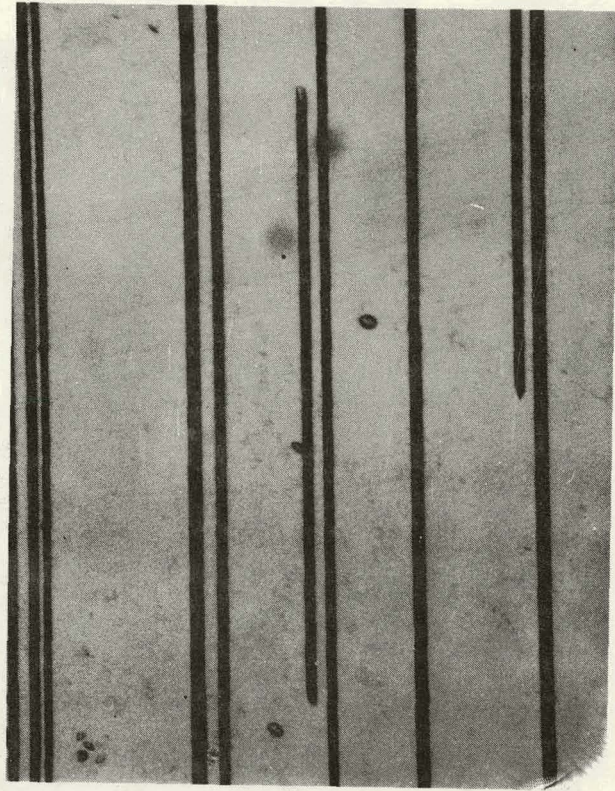
Figure 10. Stacking Fault - Surface

Figure 11. Stacking Faults - Cross-Section
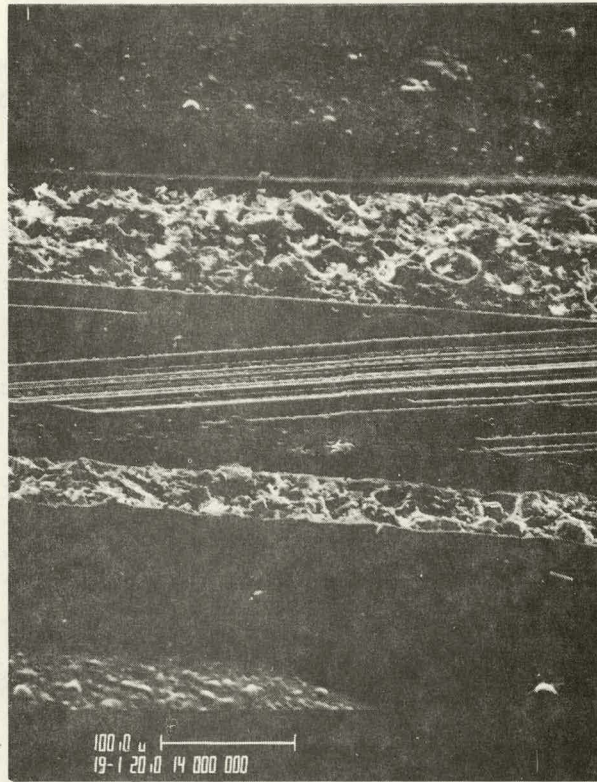
RIBBON
SECTION

Figure 12. Stacking Faults - Section Parallel to
Growth Direction

8.0 ELECTRICAL ACTIVITY OF DEFECTS

In order to specifically study the electrical activity of defects and
morphologies, an array on n+ - p photodiodes was fabricated on a few RTR
silicon ribbons. Each diode was a 1 mm x 1 mm square with a small section cut
from a corner to define the diode orientation. The total diode area was
~ 0.99×10^{-2} cm^2. The short circuit current and open circuit voltage were
measured on each of the diodes. These numbers can be used as a rough figure
of merit in evaluating the relative quality of the diodes. For comparison,
a rectangular section of a Czochralski wafer was processed along with the RTR
samples. On the Cz sample, I_{SC} ~ 150 - 160 µA and V_{OC} ~ 0.50 volts. On the
ribbon diodes I_{SC} ranged from 75 - 130 µA, and V_{OC} from 0.42 - 0.47 volts.

SEM micrographs were then taken of a selected number of diodes using the
DC Electron Beam Induced Current (EBIC) method. After the EBIC micrographs
were obtained, selected diodes were further etched for 3 minutes in Wright
etch, and optical micrographs were taken of each diode. Two diodes which
were very instructive are shown in Figures 13 - 17.

Figures 13 and 14 are EBIC and optical micrographs, respectively, of diode
12, 4 on ribbon #651. Diode 12, 4 was a relatively good performer with I_{SC} =
122 µA and V_{OC} = 0.47 volts. Close inspection of Figure 14 will reveal that
a major portion of this diode's area was covered by a dendrite. Yet the
dendrite does not appear at all in the EBIC micrograph, Figure 13. Some of
the planar defects, however, are electrically active. Yet even they are not
completely "dead" areas, and do produce some response. The linear density of
these planar defects is roughly 120/cm. In this density range, they
clearly would not have a devastating effect on the diode's photoresponse.

26
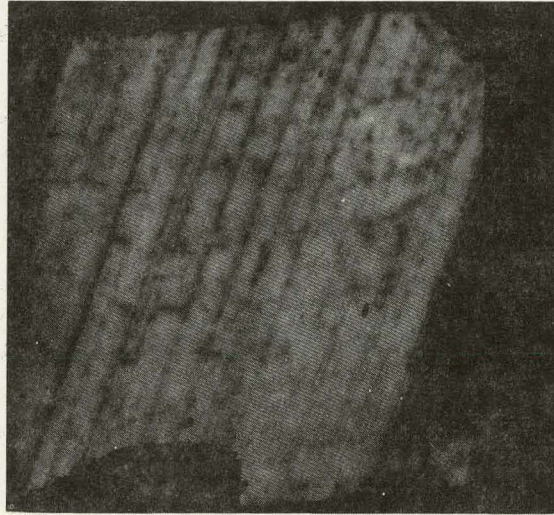
Figure 13.   EBIC Micrograph – diode 12,4
on Ribbon 651
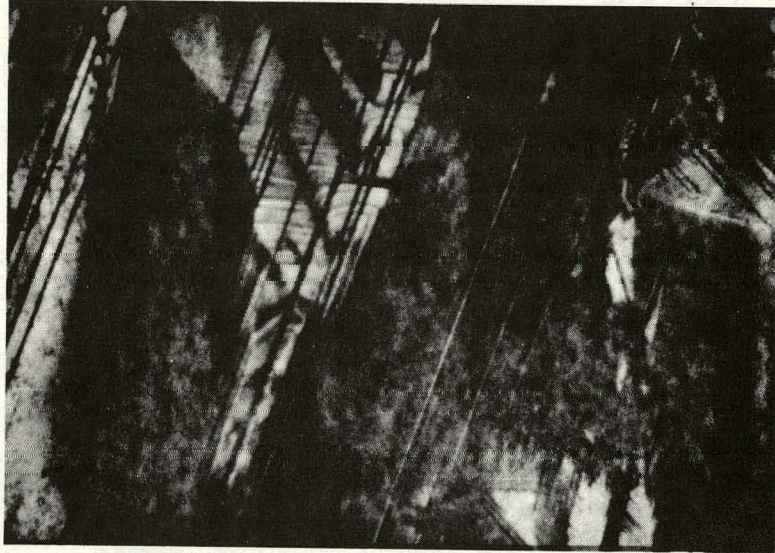
Figure 14.   Optical Micrograph - diode 12,4 on
              Ribbon 651

By contrast, diode 4,4 on ribbon #651 is a poor performer, I_{SC} = 77 μA and V_{OC} = 0.43 volts. The grain boundary (See Figure 15 at the upper left corner of the diode) is clearly a very effective recombination center. Yet the greatest part of the diode is apparently free from grain boundaries, twin planes or stacking faults. Figure 16, however, shows that the apparently clear area in diode 4,4 actually contains a very high density band of dislocations. Note that even the general pattern of the dislocations is reproduced in the EBIC micrograph. Figure 17 is a micrograph of a part (upper left) of diode 4,4, taken at a higher magnification. The dislocation density measured in the densest part of the dislocation band was $4 \times 10^6/cm^2$. For comparison, the dislocation density measured on diode 12,4 was $\sim 5 \times 10^5/cm^2$. Note that the area left of the grain boundary on Figure 17, which has excellent response in the EBIC micrograph shown in Figure 15, is relatively free of dislocations, although it does contain some non-electrically active planar defects.

These results are in fairly good agreement with our previous study on the effect of dislocation density on diffusion length (3). In that study we succeeded in correlating diffusion length with dislocation density at numerous points on an RTR ribbon. Away from grain boundaries, the dislocation density had to approach $10^6/cm^2$ in order to reduce the diffusion length below 20 μm.

We can therefore conclude:

1. Grain boundaries are often very effective recombination centers. However, their effect is limited to a very narrow area close to the boundary. Since grain boundaries typically occur with spacings of a few millimeters, they should not severely affect the generation current in solar cells. However, further processing might reveal other deleterious effects, e.g., a shunt resistance, which would degrade the cell.

29
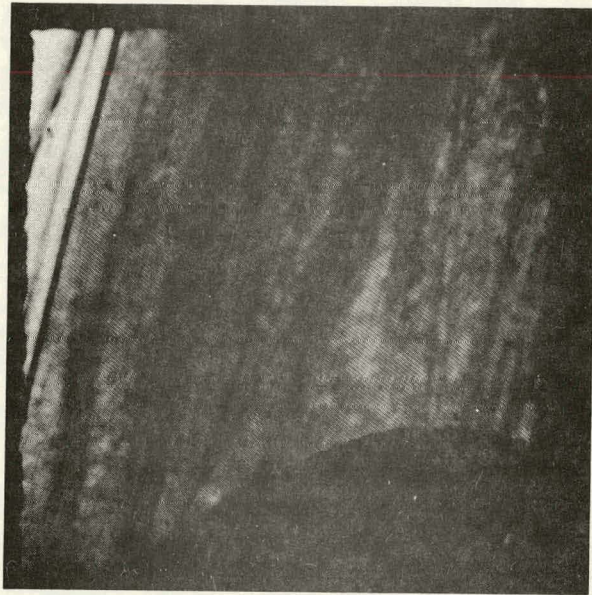
Figure 15.   EBIC Micrograph – diode 4,4 on
Ribbon 651
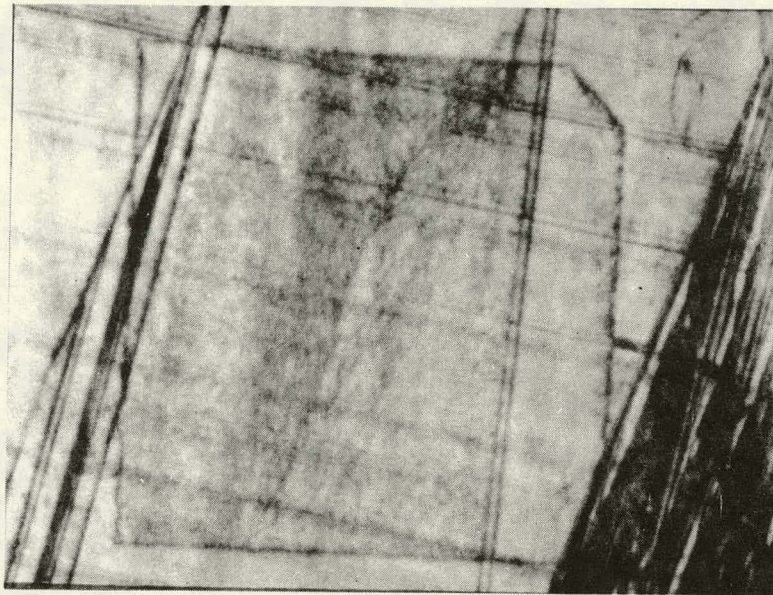
Figure 16.   Optical Micrograph - diode 4,4 on
              Ribbon 651

Figure 17.   Optical Micrograph – diode 4,4 on
            Ribbon 651

2. The ribbons are fairly tolerant of dislocations. They are a major source of poor performance only when they occur in bands with densities exceeding $10^6/cm^2$. The typical dislocation density in RTR ribbon is $2 - 5 \times 10^5/cm^2$.

3. Planar defects at density $\sim 10^2/cm$ have only a small effect on the generation current.

9.0   SOLAR CELL EVALUATION

The relocation and re-installation of our solar cell processing facilities was completed during this quarter. We can again process ribbon samples, and currently have four lots underway. We have switched from a mesa to a planar structure, using Si_3N_4 for masking. Also, we are attempting to include a back-surface field to enhance the open circuit voltage. Table 1 presents the new sequence being followed. No new cells are currently being made with the mesa structure.

We are able to report results of our first solar cell made on regrown CVD feedstock. The efficiency under simulated AM1 illumination was 6.7%, with $V_{OC} = .53V$, $J_{SC} = 24$ mA/cm^2, and fill factor = 53%. The cell area was 2.5 cm^2. A photograph of the cell (Figure 18) reveals two characteristics of this device. First, the metallization pattern is incomplete in three important areas. These breaks in the narrow fingers were caused by incomplete masking during the photoresist procedure. This flaw in processing is occasionally seen on ribbon cells, and is caused by insufficient collimation of our present photoresist exposure lamp. It is aggravated (in this case) by the extremely uneven surface as a result of the numerous dendrites.

This brings up the second characteristic of this cell, namely that it has several small dendrites running through it. The largest can be seen right at the center and crossing the main contact bus.

The incomplete metallization pattern is partially responsible for the poor fill factor that is observed. Figure 19 shows the illuminated I-V characteristics for the CVD cell. The series resistance for this device (measured by comparing dark and illuminated curves) was approximately 1 ohm, 5 - 10 times larger than normal. Using this value, the I-V curve for negligible series resistance can be calculated and is plotted as a dashed line. Note that there is a slight

34

TABLE 1

RIBBON SOLAR CELLS - PLANAR PROCESS

STEP	PROCESS
1	HF to clear
2	5:1:4 etch, Remove 2-4 µM
3	Std. clean, Si_3N_4 700Å
4	Protect front, strip back
5	BCl_3 pre-dep, 1000Å (glass)
6	Protect back, planar pattern front
7	Planar etch (HF)
8	PH_3 diffusion
9	Strip ~ 500Å of oxide
10	AR coat (850Å Si_3N_4)
11	Pattern front, strip back
12	Metallize

35
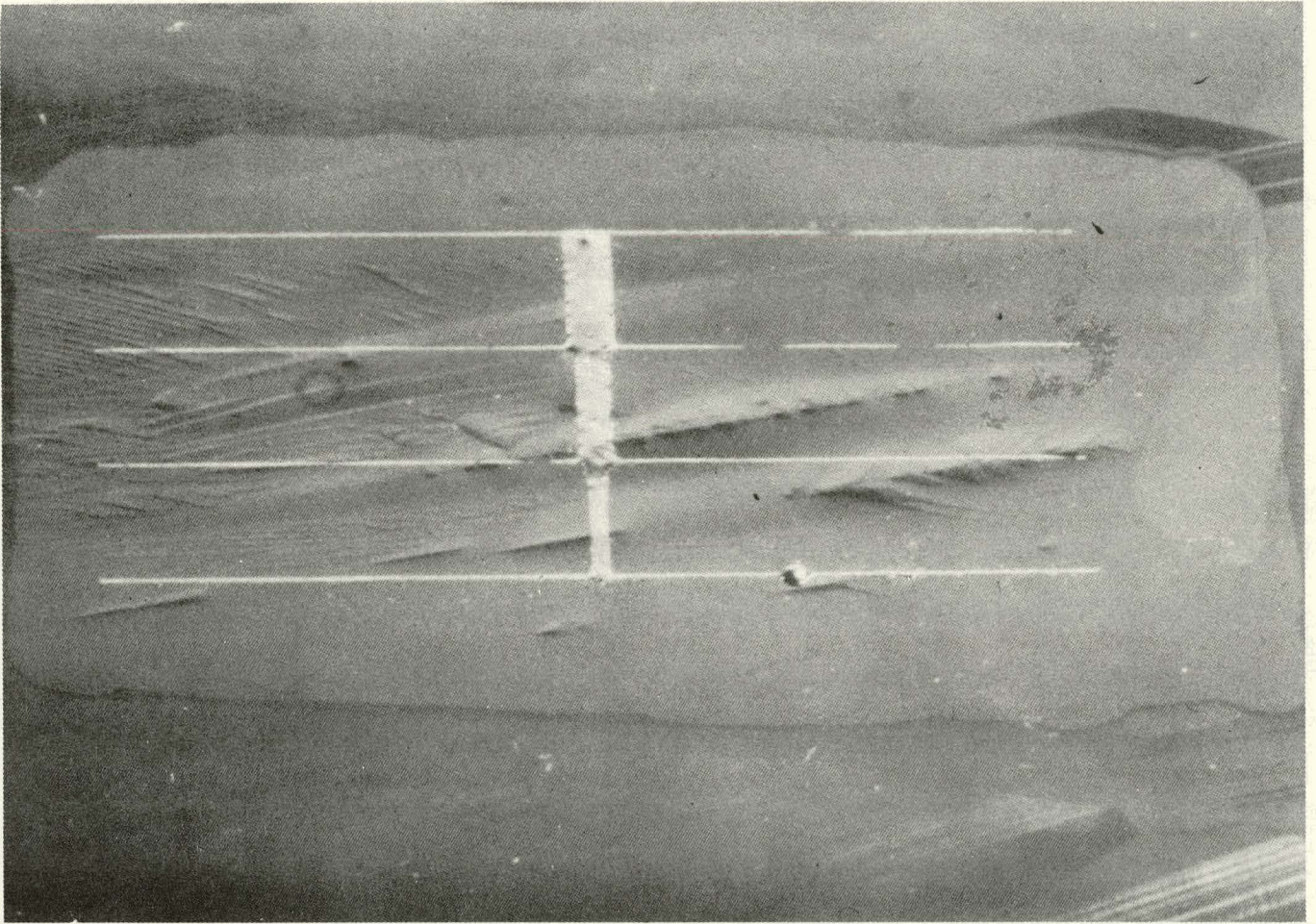
FIGURE 18: CVD SOLAR CELL

36
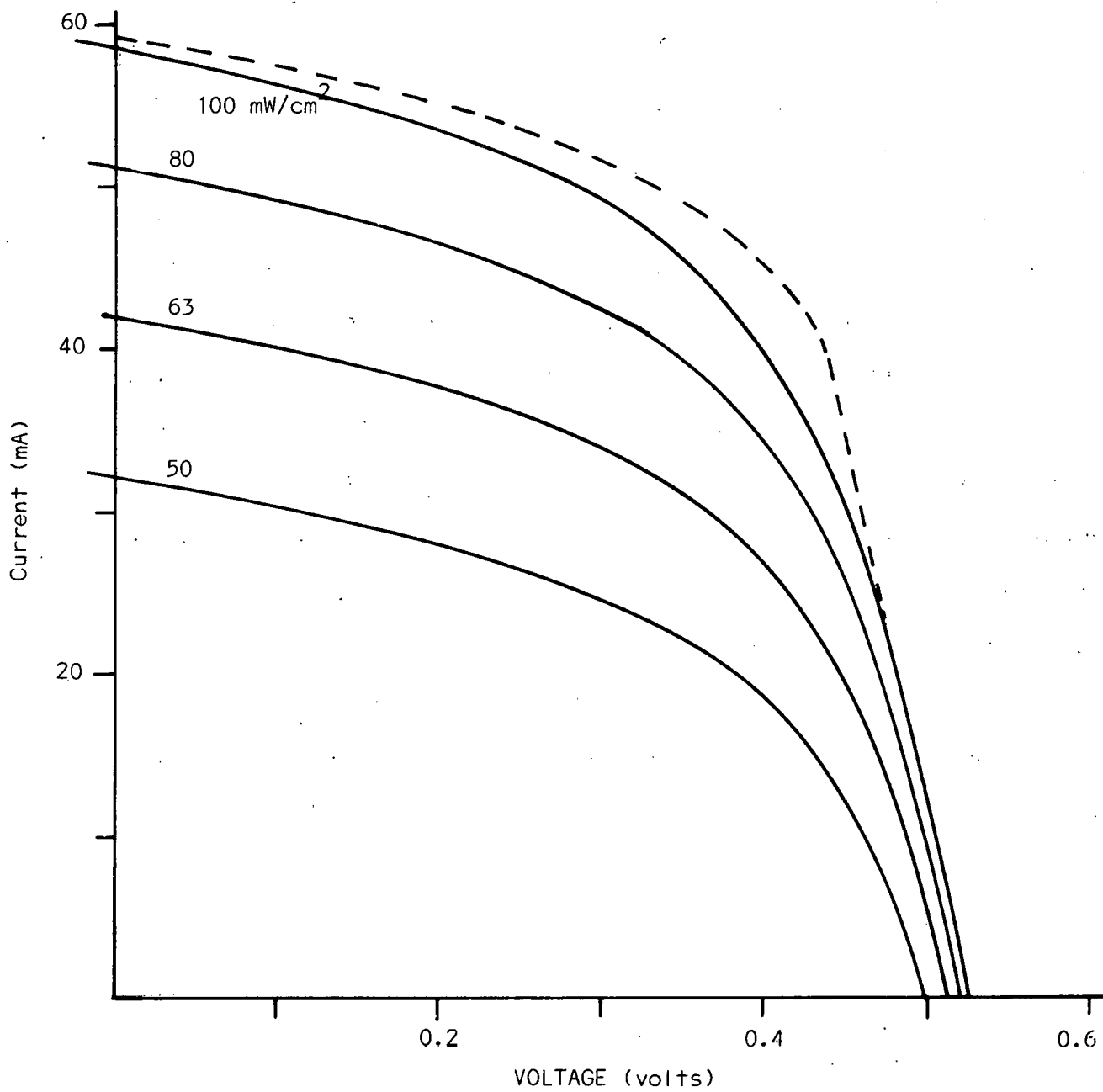
FIGURE 19:   ILLUMINATED I-V CHARACTERISTIC

37

increase in J_{SC} and a more substantial increase in the fill factor, from 53% to 57%. Of course, a fill factor of 57% is still unacceptably low, and the cause can be seen in a semilograthmic plot of the dark current-voltage characteristics (Figure 20). At voltages below about .5 volts, there is an excessive amount of leakage current. The cause of this excess current is not known at present, but it is encouraging to see a better-than-average value of V_{OC} in spite of the high dark current.

The short circuit current of 24 mA/cm^2 requires that the substrate material possess a minority carrier diffusion length in excess of 35 μM, (and possibly as high as 100 μM) indicating that regrown CVD material can be gettered.

Finally, we have successfully processed a full length ribbon (9") without breakage. This ribbon (See Figure 21) is heavily dendritic and was grown from single crystal feedstock. Because of the roughness of the surface and our relative inexperience with this type of material, some of the contact patterns did not open up properly for metallization. Nevertheless, as is shown in Figure 21, a complete finger pattern can be opened up on dendritic material. Note also the small piece which has been chipped off; this breakage occurred only in the non-dendritic region and stopped at the edge of the dendrites, graphic proof of the increase in strength provided by dendritic ribbon.
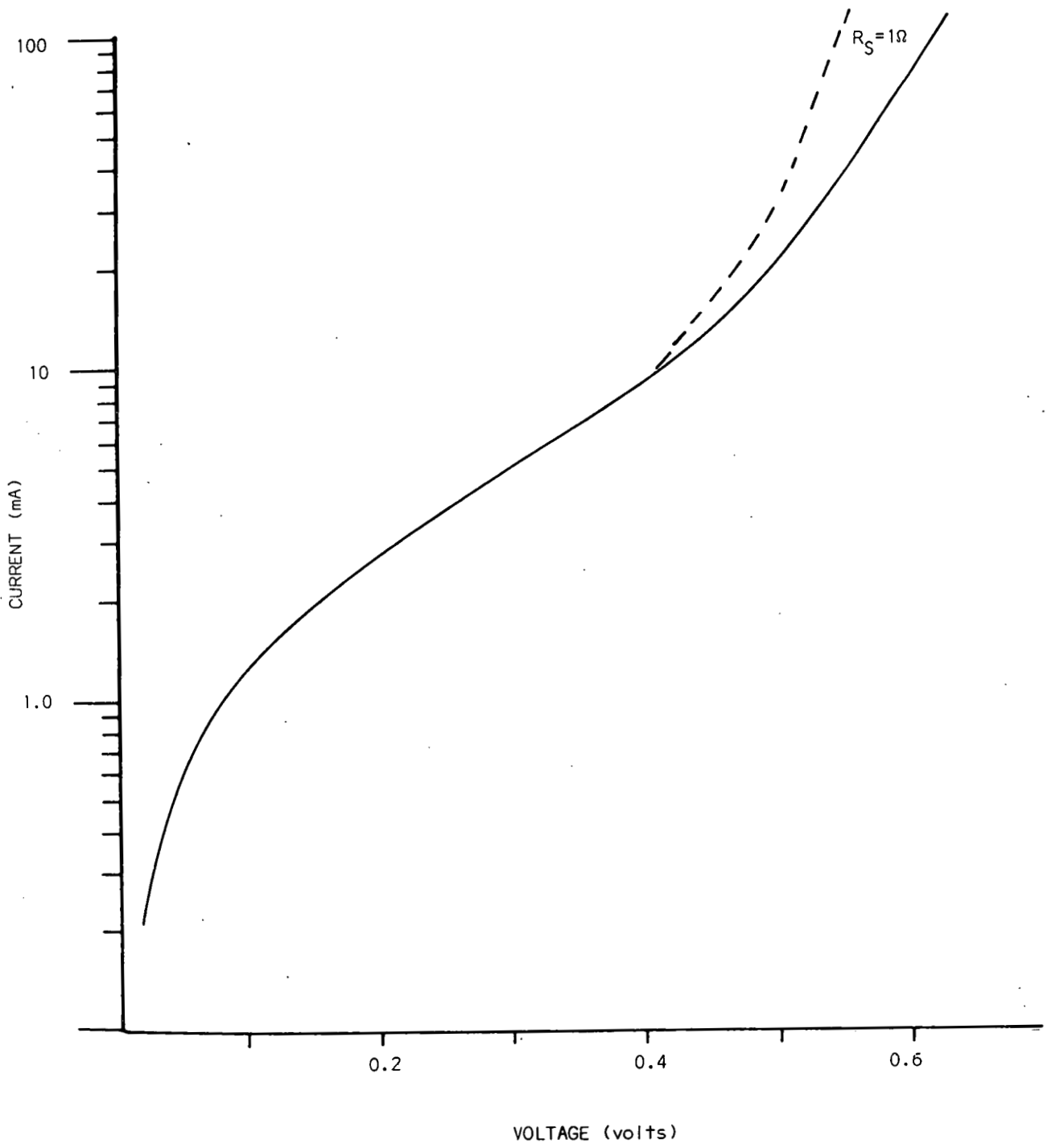
FIGURE 20: DARK I-V CHARACTERISTIC

39
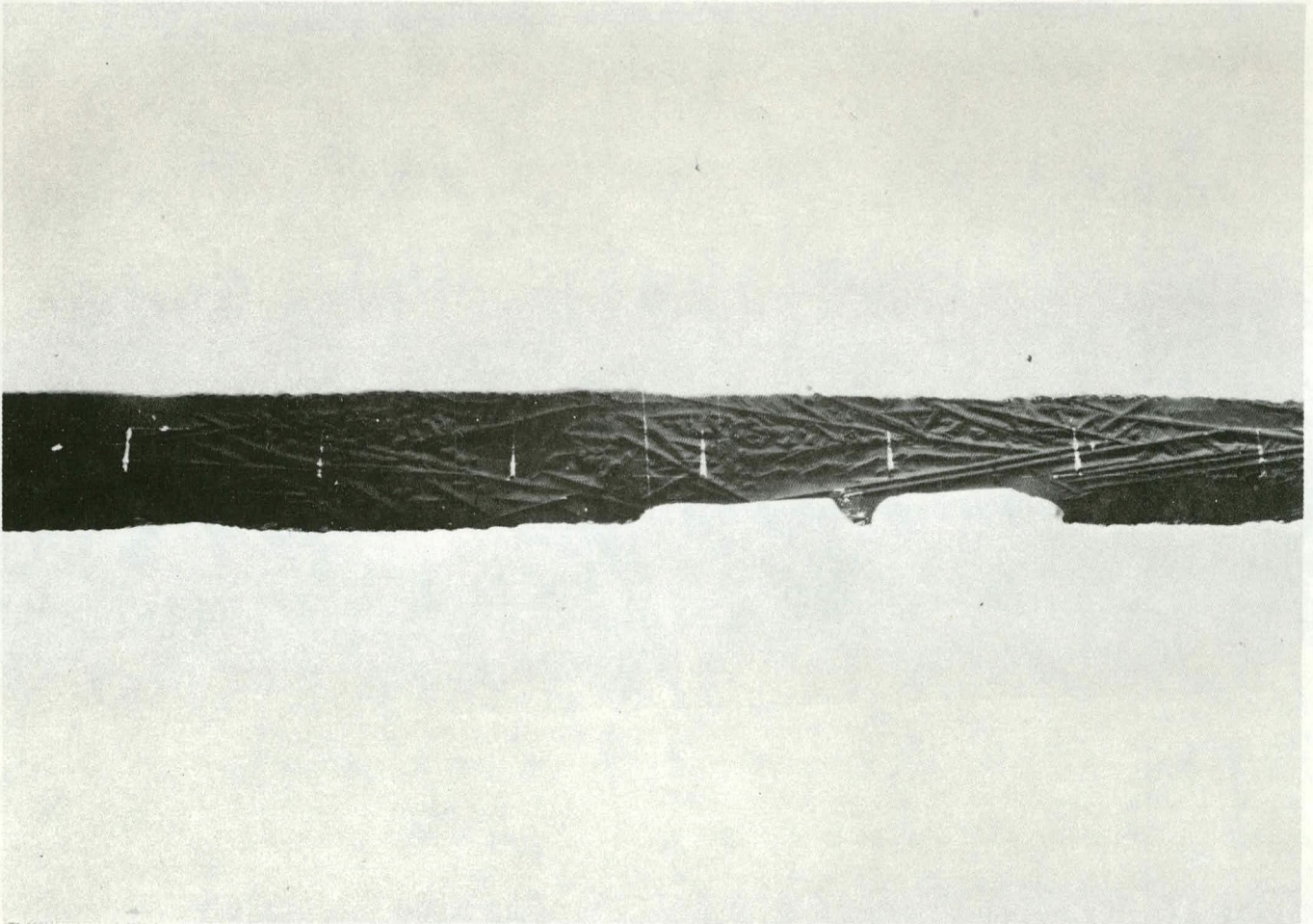
FIGURE 21: PROCESSED DENDRITIC RIBBON

40

10.0   NEUTRON ACTIVATION ANALYSIS

Table 2 shows the results of Neutron Activation Analysis on some CVD and RTR samples. These analyses were carried out by General Activation Analysis, Inc., San Diego, California. We have previously (4) reported an impurity profile obtained using SIMS (Secondary Ion Mass Spectroscopy) analysis. The surface concentration of molvbdenum determined by SIMS was 5 ppm, and it dropped off to the detection limit (< 0.5 ppm) within a depth of 1 μm from the surface. The Neutron Activation results reported here imply roughly an order of magnitude higher Mo contamination than the SIMS analysis.

These results show that we are getting a relatively high level of Mo into the RTR samples. The Mo is probably not concentrated exclusively at the back surface, but is spread through the bulk of the silicon. Note, however, that some of the differences seen in Table 2 may be due to sample-to-sample variations rather than to the specific sample history.

These results are rather puzzling in light of the Westinghouse (5) results: Mo at a concentration of even < 10^{12} ppm seriously degrades the performance of Si photovoltaic cells. Yet, in Section 9.0 we reported on a CVD cell, presumably containing 5 - 10 ppm of Mo, which was a fairly good performer, particularly with V_{OC} (0.53V) and I_{SC} (24 mA/cm^2). The V_{OC} is actually higher than the typical values we have been measuring on cells fabricated on RTR ribbons grown from single crystal feedstock. The I_{SC} is lower by 15% - 20%, -- which is the degradation Westinghouse observed for a 10^{12}/cm^3 Mo concentration. Thus, it is possible that Mo as an impurity in RTR ribbon behaves differently than Mo in a Cz single crystal. Possibly the Mo is being accumulated at certain defects, perhaps in the form of an oxide. Further investigation on solar cells fabricated on CVD feedstock RTR silicon should help resolve this question.

TABLE 2

NEUTRON ACTIVATION ANALYSIS

SAMPLE #	DESCRIPTION	Mo (ppm)	W (ppm)
1	RTR ribbon, grown from single crystal feedstock	N.D. <.088	N.D. <0.0016
2	CVD ribbon (as deposited)	6.66	.0093
3	RTR ribbon, grown from CVD feedstock	12.5	.025
4	CVD ribbon (2 mils etched from surface which was in contact with Mo substrate)	5.60	.00661
5	Plasma deposited ribbon (as deposited)	3.37	N.D. <0.0011

N.D.   Not Detected.   The upper limits are based on three standard deviations from counting statistics.

11.0   PROBLEMS

Neutron activation analysis on CVD ribbon has shown a high (5 - 10 ppm) level of Mo impurity. However a solar cell fabricated on RTR ribbon grown from this feedstock indicates that this impurity level is not necessarily a serious problem.

12.0   PLANS

1. CVD Feedstock - Continue producing $1\frac{1}{4}$" x 9" feedstock. Start growth of semicontinuous silicon ribbon; start night shift.

2. Crystal Growth - In addition to routine growth of $1\frac{1}{4}$" wide ribbon from CVD feedstock, we will work on faster growth of wider (2" - 3") ribbons.

3. Stress Analysis - We will implement the computer program to calculate the thermal stress distribution as a function of various temperature profiles.

4. Solar Cells - Evaluate solar cells built on CVD feedstock. We will also consider the effects of the new planar/Si_3N_4 process sequence.

13.0   NEW TECHNOLOGY

The following New Technology item has been developed on this program:

1. Description - Polygon Scanner System

   Innovator - Dr. Richard Gurtler

   Progress Reports - Technical Progress Report No. 14 October 1977

   Pages - Pages 1, 10, 11A, and 11

2. Description: Hemispherical Reflector to Improve Effective Absorption Coefficient of Liquid Silicon

   Innovator: Dr. Richard Gurtler

Progress Reports: Technical Quarterly Report No. 7,

Motorola Report 255619, 1 January 1978 – 31 March 1978,

Pages – Appendix Pages 11–13

14.0   <u>MILESTONE CHART</u>

Activities associated with the total program are shown in the

Milestone chart contained in the Appendix.

REFERENCES

1. Boley and Weiner, <u>Theory of Thermal Stresses</u>, John Wiley & Sons, N. Y. 1960, p. 261.

2. L. C. Gerone, et. al. Appl. Phys. Letters, <u>29</u>, (1976) p. 511.

3. R. W. Gurtler, et. al., Technical Quarterly Report #6, DOE/JPL 954376-78/1 (1978).

4. K. R. Sarma, et. al., Quarterly Report *4, "Thin Films of Silicon on Low-Cost Substrates", Dec. 1977, DOE Contract No. EY-76-C-03-1287.

5. Reported by Westinghouse at the IXth LSA Project Integration Meeting, JPL, Pasadena, California, April, 1978.
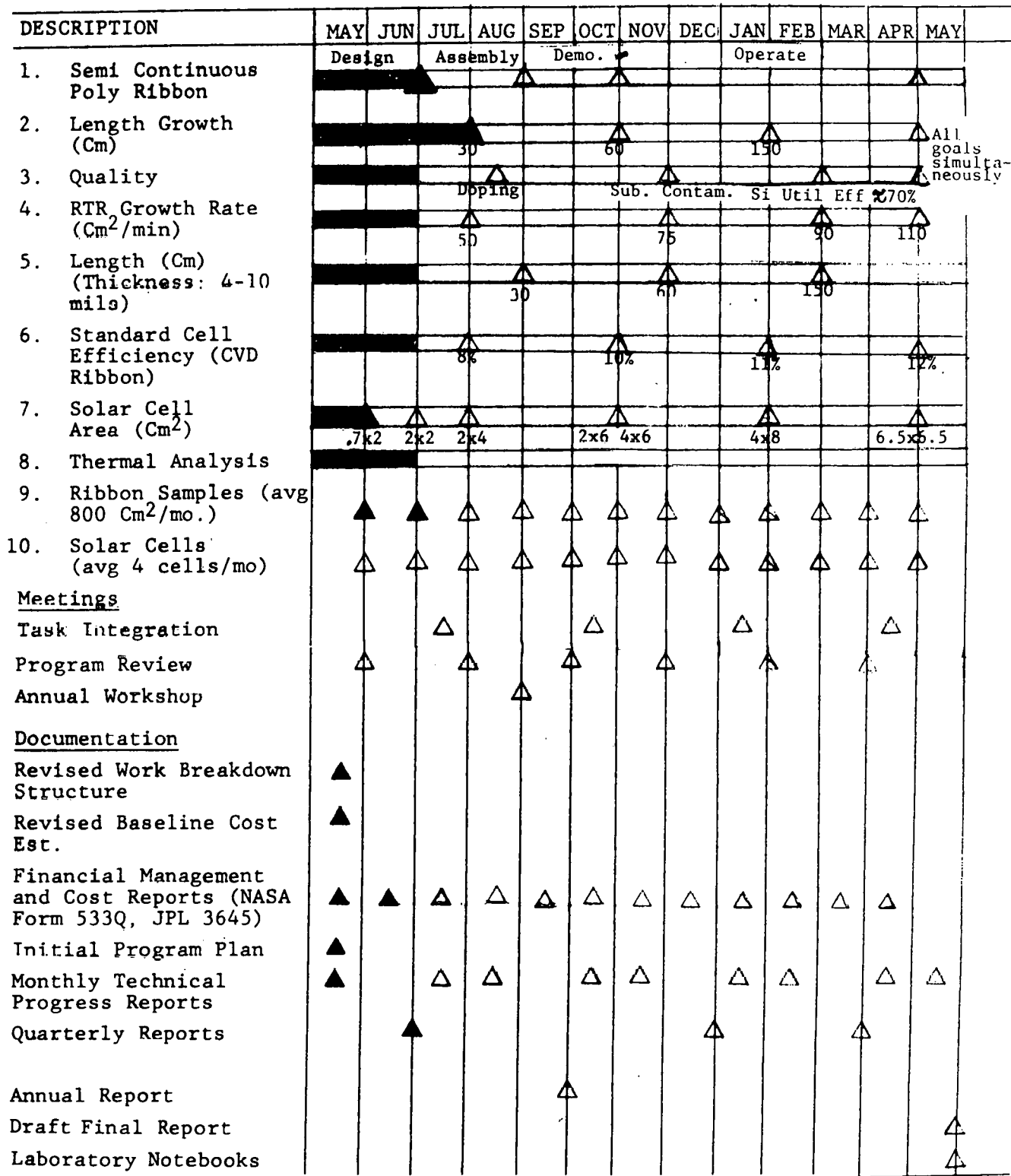
THIS PAGE

WAS INTENTIONALLY

LEFT BLANK

APPENDIX

MILESTONE CHART

Contract No. 954376   MOTOROLA PROJECT NO. 2319-2325

DESCRIPTION	MAY	JUN	JUL	AUG	SEP	OCT	NOV	DEC	JAN	FEB	MAR	APR	MAY
	Design		Assembly		Demo.				Operate				
1. Semi Continuous Poly Ribbon	▓	▓	△		△							△	
2. Length Growth (Cm)	▓	▓	30		60 △				150 △			△ All goals simulta- neously	
3. Quality	▓	▓	△		△				△			△	
			Doping			Sub. Contam.			Si Util Eff % 70%				
4. RTR Growth Rate (Cm^2/min)	▓	△ 50				△ 75				△ 90		△ 110	
5. Length (Cm) (Thickness: 4-10 mils)	▓		△ 30			△ 60				△ 150			
6. Standard Cell Efficiency (CVD Ribbon)	▓		△ 8%			△ 10%				△ 11%		△ 12%	
7. Solar Cell Area (Cm^2)	▓ .7x2	△ 2x2	△ 2x4		△ 2x6 4x6				△ 4x8			△ 6.5x6.5	
8. Thermal Analysis	▓												
9. Ribbon Samples (avg 800 Cm^2/mo.)	▲	▲	△	△	△	△	△	△	△	△	△	△	
10. Solar Cells (avg 4 cells/mo)	△	△	△	△	△	△	△	△	△	△	△	△	

Meetings

	MAY	JUN	JUL	AUG	SEP	OCT	NOV	DEC	JAN	FEB	MAR	APR	MAY
Task Integration			△		△				△		△		
Program Review	△		△		△		△		△		△		
Annual Workshop				△									

Documentation

	MAY	JUN	JUL	AUG	SEP	OCT	NOV	DEC	JAN	FEB	MAR	APR	MAY
Revised Work Breakdown Structure	▲												
Revised Baseline Cost Est.	▲												
Financial Management and Cost Reports (NASA Form 533Q, JPL 3645)	▲	▲	△	△	△	△	△	△	△	△	△	△	
Initial Program Plan	▲												
Monthly Technical Progress Reports	▲		△	△		△	△		△	△		△	△
Quarterly Reports			▲					△			△		
Annual Report					△								
Draft Final Report												△	
Laboratory Notebooks												△	

LEGEND ☐ SCHEDULE   COMPLETED   DELIVERY SCHEDULE △   DELIVERED ▲

48